

Qimei Gu

Department of Mechanical Engineering,
University of Maryland Baltimore County,
Baltimore, MD 21250
e-mail: qg1@umbc.edu

Shuaishuai Liu

Department of Biology,
University of Maryland Baltimore County,
Baltimore, MD 21250
e-mail: lius1@umbc.edu

Arunendra Saha Ray

Department of Chemistry and Biochemistry,
University of Maryland Baltimore County,
Baltimore, MD 21250
e-mail: arun5@umbc.edu

Stelios Florinas

Department of Antibody Discovery and
Protein Engineering,
AstraZeneca R&D,
Gaithersburg, MD 20878
e-mail: Stelios.florinas@immunocore.com

Ronald James Christie

Department of Antibody Discovery and
Protein Engineering,
AstraZeneca R&D,
Gaithersburg, MD 20878
e-mail: christier@medimmune.com

Marie-Christine Daniel

Department of Chemistry and Biochemistry,
University of Maryland Baltimore County,
Baltimore, MD 21250
e-mail: mdaniel@umbc.edu

Charles Bieberich

Department of Biology,
University of Maryland Baltimore County,
Baltimore, MD 21250
e-mail: bieberic@umbc.edu

Ronghui Ma

Department of Mechanical Engineering,
University of Maryland Baltimore County,
Baltimore, MD 21250
e-mail: roma@umbc.edu

Liang Zhu¹

Department of Mechanical Engineering,
University of Maryland Baltimore County,
Baltimore, MD 21250
e-mail: zliang@umbc.edu

Mild Whole-Body Hyperthermia-Induced Interstitial Fluid Pressure Reduction and Enhanced Nanoparticle Delivery to PC3 Tumors: In Vivo Studies and Micro-Computed Tomography Analyses

In this study, we performed in vivo experiments on mice to evaluate whether whole-body hyperthermia enhances nanoparticle delivery to PC3 (prostatic cancer) tumors. PC3 xenograft tumors in immunodeficient mice were used in this study. The mice in the experimental group were subjected to whole-body hyperthermia by maintaining their body temperatures at 39–40 °C for 1 h. Interstitial fluid pressures (IFPs) in tumors were measured before heating, immediately after, and at 2 and 24 h postheating in both the experimental group and in a control group (without heating). A total of 0.2 ml of a newly developed nanofluid containing gold nanoparticles (AuNPs) was delivered via the tail vein in both groups. The micro-computed tomography (microCT) scanned images of the resected tumors were analyzed to visualize the nanoparticle distribution in the tumors and to quantify the total amount of nanoparticles delivered to the tumors. Statistically significant IFP reductions of 45% right after heating, 47% 2 h after heating, and 52% 24 h after heating were observed in the experimental group. Analyses of microCT scans of the resected tumors illustrated that nanoparticles were more concentrated near the tumor periphery rather than at the tumor center. The 1-h whole-body hyperthermia treatment resulted in more nanoparticles present in the tumor central region than that in the control group. The mass index calculated from the microCT scans suggested overall 42% more nanoparticle delivery in the experimental group than that in the control group. We conclude that 1-h mild whole-body hyperthermia leads to sustained reduction in tumoral IFPs and significantly increases the total amount of targeted gold nanoparticle deposition in PC3 tumors. The present study suggests that mild whole-body hyperthermia is a promising approach for enhancing targeted drug delivery to tumors. [DOI: 10.1115/1.4046520]

Keywords: hyperthermia, EPhA2, gold nanoparticle, drug delivery to tumors, IFP reduction, bioheat transfer, microCT, bioheat and mass transfer, micro/nanoscale heat transfer

1 Introduction

In recent years, advancements in nanotechnology have revolutionized cancer treatment as a part of therapeutic intervention. Currently, different types of nanoparticles are being evaluated as

imaging contrast agents [1,2], absorptive heating agents to confine heat in targeted tumors [3,4], and carriers of therapeutic agents [5,6]. Among those functions, therapeutic drugs attached to the surfaces of nanocarriers or embedded within hollow nanostructures have great potential for tumor-targeted delivery with prolonged circulation time and reduced systemic toxicity. Additionally, previous studies [5,6] have shown that those nanostructures can load sufficient amounts of drug molecules and improve biocompatibility. Once the drug reaches the tumor region, nanostructures can

¹Corresponding author.

Manuscript received September 23, 2019; final manuscript received February 25, 2020; published online June 16, 2020. Assoc. Editor: Hongbin Ma.

be used to control drug release to achieve a desirable drug concentration for a prolonged duration, thereby avoiding concentration bursts often seen in treatments.

For most cancer treatments, drugs are delivered either orally or via intravenous (i.v.) injection. For an i.v. administration, therapeutic agent delivery often uses ligand-conjugated nanostructures. The ligand (e.g., antibody, Fab fragment) can bind to cell surface receptors exclusively overexpressed in tumors, resulting in a high accumulation of drugs in the targeted tumor [7]. Once the drug reaches the capillaries in the tumor, it has to pass through pores in the capillary membrane due to pressure differences and then diffuse through the interstitial space before it finally enters the tumor cells. Nanostructure transport from tumor capillaries to the tumoral interstitial space remains difficult. Within tumors, the elevated interstitial fluid pressure (IFP), dense extracellular matrix, high cell density, and possible blockage of tumor vascular fenestrations by nanoparticles present additional barriers that may impede efficient delivery to tumor cells. Thus, only a very small fraction of the injected nanoparticles will effectively enter tumor cells, resulting in poor and heterogeneous delivery of the drug. Among these potential barriers, the high tumor IFP is a major obstacle for drug delivery [8].

Vascular permeability in tumors is typically higher than that in normal tissues due to the irregular and loose structure of the neoplastic endothelium [9]. Previous studies have explored how heat-induced permeability enhancement boosts drug/nanostructure extravasation from blood vessels into the tumor interstitial space in systemic drug delivery [10–12]. Possible mechanisms of local heating including endothelial thermal stress/injury and transient thermal damage to the cellular homeostatic mechanism have been suggested as a means to increase nanoparticle extravasation and penetration into the interstitial space.

Governed by Starling's law, extravasation of fluid from capillaries is directly related to the pressure difference between the capillary and the interstitial fluid; thus, passive advection of nanoparticles is hindered by the high IFP in tumors. IFP in tumors is usually elevated due to the formation of irregular and leaky vasculature in the early stages of uncontrollable and rapid cell proliferation as well as the lack of a well-developed lymphatic system. In studies by Dr. R. Jain's group, they implemented an anti-angiogenesis treatment to normalize tumor vasculature, which significantly decreased the interstitial fluid pressure [13]. However, the normalization process also reduced the size of fenestrations in the capillary walls, thus limiting the size of the nanoparticles to less than 12 nm if this approach were to be effective. A 2011 study by Sen et al. [14] was the first investigation on utilizing mild whole-body hyperthermia to improve the tumor microenvironment. They proposed that mild whole-body hyperthermia would trigger thermoregulatory responses to change flow patterns in the blood vessels upstream or downstream of the tumor vasculature, and this would result in reduced interstitial fluid pressure in tumors. In that study, both murine colon tumors and murine melanomas implanted in mice demonstrated significantly smaller IFPs in the tumors when the mice were subject to 2 h, 4 h, or 6 h of whole-body heating, when compared to the control group that did not undergo heating. This experimental study established correlations among IFP reductions, increases in local tumoral blood perfusion, and reductions in tumor hypoxia. Later, a study by Winslow et al. [15] tested the same approach in mouse models bearing human head and neck tumor xenografts. After 4 h of whole-body hyperthermia, the interstitial fluid pressure in the tumors decreased by 23% compared to the control, and this reduction was maintained for more than 24 h. Using fluorescent liposomes circulating in the blood stream, they found that heating opened many blood vessels in the tumors, and they visualized enhanced liposome extravasation using fluorescence microscopy of frozen tumor sections [15]. Both studies also illustrated that whole-body hyperthermia improved the treatment efficacy of radiation therapy by showing significant inhibition of tumor growth. It is unclear whether the observed phenomena in the previous studies are applicable to other tumors since thermal

responses may vary among different tumor models. Another unanswered question is whether implementing a shorter heating duration (1 h of mild whole-body hyperthermia) into a different kind of tumors would achieve similar interstitial fluid pressure reductions. This is in consideration of a patient's thermal tolerance in future clinical studies.

Typical experimental approaches for evaluating drug/nanostructure distribution in tumors utilize fluorescently labeled drug molecules in implanted tumors in animal models [10,16,17]. Due to the penetration limitation of confocal microscopy ($\sim 200 \mu\text{m}$ in depth) and other optical methods, drug transport in the interstitial space of tumors was evaluated via a two-dimensional (2D) cranial or dorsal window chamber tumor preparation [10,11]. The complicated heterogeneous three-dimensional (3D) tumor structure may not be well represented in a 2D tumor preparation, and the 3D drug transport process is often not completely captured by those approaches. Recently, micro-computed tomography (microCT) imaging techniques have been proposed as a noninvasive and non-destructive method for investigating nanoparticle distribution in tumors. Although microCT does not allow direct visualization of individual nanoparticles, the accumulation of nanoparticles in tissue would result in a region with a much higher density than the rest of the tissue; thus, the density variations can be detected by a microCT system [18–20]. Several recent studies [18–20] have shown the feasibility of imaging and quantifying detailed 3D nanoparticle distribution in both gels and tumors. From those microCT images, it is evident that the nanoparticles are mostly confined to the vicinity of the injection site after an intratumoral injection, and the nanoparticle distribution volume in the tumor can be calculated with high precision. Therefore, microCT scans of resected tumors after whole-body hyperthermia have the potential to provide mapping of 3D nanoparticle deposition in tumors. Grayscale (GS) values in microCT scan would also be useful in quantifying local nanoparticle concentration distribution in tumors.

In this study, we tested the hypothesis that 1-h whole-body hyperthermia may lower tumor IFP to allow more nanoparticles to be deposited into PC3 tumors after a systemic injection. In vivo experiments were performed to evaluate the effects of whole-body hyperthermia on the deposition of nanoparticles in PC3 tumors in mice. Gold nanoparticles (AuNPs) coated with ligands that specifically target EphA2 receptors on PC3 tumor cells were developed to enhance cancer cell uptake of nanoparticles as previously described [2]. A total of 0.2 ml of the prepared nanofluid was injected through the tail vein with or without 1-h whole-body hyperthermia. During the experiments, mouse body temperatures and tumor IFPs at various time points were also measured. MicroCT scans of resected tumors were performed to analyze and visualize local nanoparticle concentration distribution and to calculate the total amount of nanoparticle deposition in the PC3 tumors.

2 Methods

2.1 Nanoparticle Preparation. Figure 1 shows the synthetic scheme for the preparation of the nanofluid (highly concentrated aqueous solution of AuNPs functionalized with Fab fragments for specific targeting of PC3 cells). First, gold nanoparticle cores (AuNP-citrate) were formed following a procedure adapted from the study by Zabetakis et al. [21]. Briefly, a gold chloride solution was prepared by dissolving HAuCl_4 (0.1 g in 1000 ml) to give a 0.3mM Au^{3+} solution. Sodium citrate stock solution (0.17M) was prepared by dissolving 1.3 g sodium citrate in 20 ml water. The gold salt solution was heated to reflux using an oil bath. Once reflux was reached, the entirety of the sodium citrate stock solution (20 ml) was added at once to the reaction mixture under vigorous stirring. The gold salt-to-citrate molar ratio used was 1:10. After 1 h under reflux, the AuNP-citrate solution was cooled to room temperature.

The AuNP-citrate was then coated with a polypropyleneimine (PPI) dendron (TA-TEG-G3CO₂H) previously developed in our

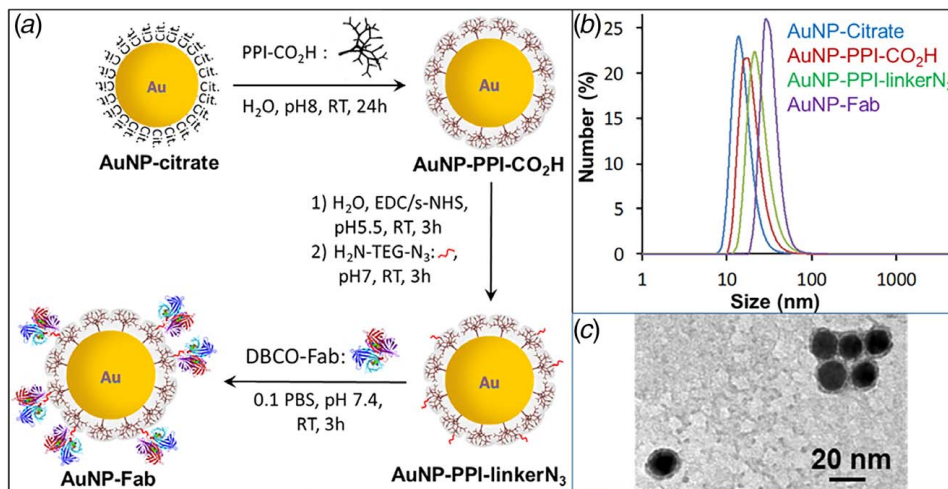


Fig. 1 (a) Synthetic scheme for the preparation of the nanofluid solution (AuNP-Fab), (b) size measurements (DLS by number) of the three AuNP intermediates in water and of the final AuNP-Fab in 0.05 PBS solution, and (c) representative image of AuNP-Fab using TEM with negative staining

labs [22]. For this, 250 mg (20 times molar excess of AuNP thiol coverage) of the TA-TEG-G3CO₂H dendron dissolved in water (pH 8) was added to 1 l of AuNP-citrate solution and stirred for 1 day at room temperature. The dendronized AuNPs were then centrifuged in four coming containers (300 ml flask) at 12,000 g, 5 °C, 90 min to generate a pellet. The supernatant was carefully pipetted out and the pellet was resuspended in 200 ml pH 8 water. The concentrated AuNP-PPI-CO₂H solution was further centrifuged at 12,000 g, 5 °C for 90 min, and the supernatant was discarded. The pellet was then redispersed in pH 8 water (20 ml) and set for dialysis (MWCO (molecular weight cut-off), 12,000 Da). The dialysis water was changed every 4 h for a total dialysis time of 12 h. To 30 ml of AuNP-PPI-CO₂H solution (3 mg/ml), 1.6 mg (160 μl of 10 mg/ml stock) of EDC (1-ethyl-3-(3-dimethylamino-propyl)carbodiimide) was added at pH 5.5 followed by immediate addition of 3.2 mg (320 μl of 10 mg/ml) of s-NHS. The resulting solution was allowed to stir for 3 h at room temperature. After 3 h, 8.6 mg of H₂N-TEG-N₃ linker (100 μl stock of 85 mg/ml) was added to the solution, and pH was adjusted to 7 by addition of 50 μl NaHCO₃ saturated solution and allowed to stir for 3 h. After 3 h, excess unconjugated linker was removed by discarding the supernatant from three consecutive rounds of centrifugation at 12,000 g, 6 °C for 40 min. Zeta potential was taken to assess the conjugation of the linker. Postremoval of excess spacer, the AuNP-PPI-linkerN₃ was dissolved in 25 ml of 0.1X phosphate-buffered saline (PBS) and functionalized with anti-EphA2 Fab fragments (also known as 1C1 Fab) provided by AstraZeneca (Gaithersburg, MD). For this functionalization, 1.3 mg (enough for 40% surface coverage of AuNP) of Fab-dibenzocyclooctyne (DBCO) (Fab fragment derivatized with DBCO, for click chemistry conjugation), was added and allowed to stir overnight at room temperature [23]. The next day, unreacted Fab-DBCO was removed from the solution by two consecutive rounds of centrifugation at 15,000 g, 10 °C for 25 min. The resulting pellet was dissolved in 9 ml of 1X PBS to generate the final AuNP-Fab construct to be used in our systemic nanofluid delivery study. The concentration of the nanofluid was 10 mg-Au/ml, and Fab attachment was confirmed by dynamic light scattering (DLS) and transmission electron microscopy (TEM) with negative staining (2% uranyl acetate).

2.2 Tumor Implantation and In Vivo Animal Experiment.

PC3 xenograft tumors were implanted in 14 Balb/c Nu/Nu male mice (28–32 g, The Jackson Lab, Bar Harbor, ME), with one tumor in each mouse, similar to our previous experiments [18–

20]. A PC3 cell solution containing 5×10^6 cells was injected into the left flank of the mouse using a 27-gauge needle (Tuberculin Syringe w/Needle by BD, Fischer Scientific, Springfield, NJ). The tumor size was estimated using a Vernier caliper, and the growth of the tumor was monitored three times a week until it reached 10 mm in the transverse diameter, which usually took 4–6 weeks. The tumor-bearing mice were randomized into two groups: the control (sham) group without whole-body heating ($n = 7$) and the experimental group with 1-h whole-body heating ($n = 7$).

Mouse body temperature was monitored by a temperature reader (Bio Medic Data Systems, Seaford, DE) implanted subcutaneously above the mouse shoulder 48 h before the experiment. Mouse temperatures were measured using a scanner to activate the temperature sensor, and then the reading was transferred to a computer. All the mice in the heating group were given an intraperitoneal (i.p.) injection of 1 ml of saline 30 min before heating to prevent dehydration. This is based on an assumption that the hydration level in the hyperthermia group by the end of the heating period is the same as that in the control group, therefore, to maintain a normal hydration status of the mice in both groups. The experimental design is illustrated in Fig. 2. One mouse in the control group and the other in the experimental group were brought to the lab side by side. As shown in

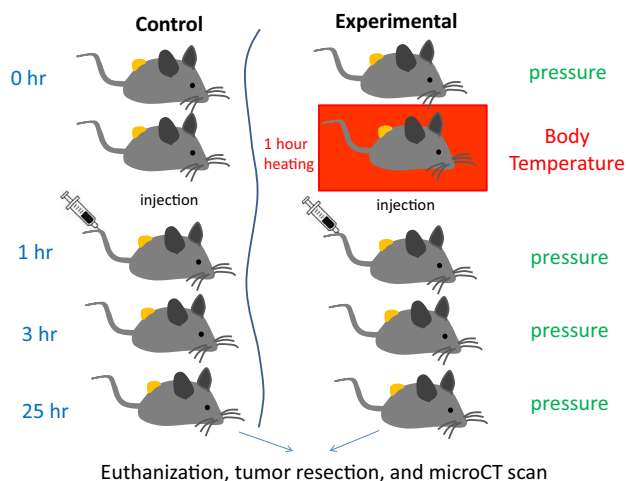


Fig. 2 Schematic diagram of the in vivo experimental protocol. Measurements are performed side by side on a mouse from the control group and a mouse from the experimental group.

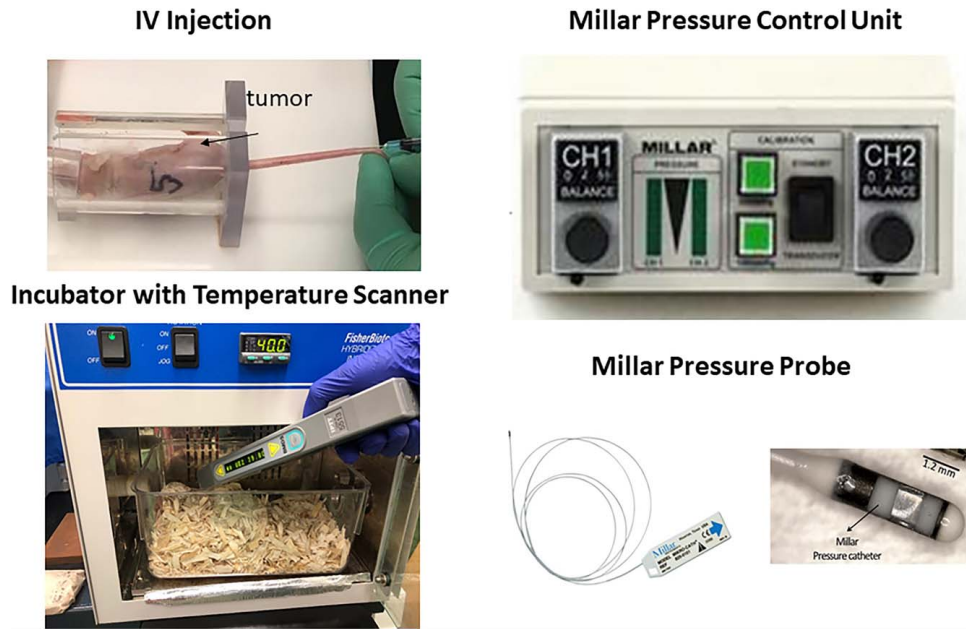


Fig. 3 Equipment used in the experiments

Fig. 3, the mouse in the experimental group was placed in a pre-heated cage within an incubator set at 39 °C for 1 h, during which the mouse in the control group is in a cage in ambient environment. The mouse body temperature was measured every 5 min during the 1-h heating duration. The cover of the incubator was open briefly for 5 s to allow insertion of the scanner to collect the temperature value. This only led to a slight decrease of approximately 0.1–0.3 °C in the air temperature inside the cage.

After the 1-h heating, 200 μl of the prepared nanofluid (10 mg-Au/ml) was injected into the mouse circulatory system via the tail veins of both mice, as shown in Fig. 3. Both mice were later sent back to the animal facility. Twenty-four hours following the nanofluid injection, the mice were brought back to the lab and euthanized using Na pentobarbital overdose (160 mg/kg, i.p.). The tumor was resected and immediately scanned by a microCT imaging system (Skyscan 1172, Micro Photonics, PA) [18–20].

During the experiments, tumor IFP was measured by a micro-pressure transducer with a probe tip size of 0.33 mm (Model SPR-1000, ADInstruments, Houston, TX), as shown in Fig. 3. Signals from the probe were first interfaced to a pressure control unit (PCU-2000, ADInstruments) and then to an analog-to-digital converter (ASA-P220, MicroMed, Louisville, KY). The IFP probe was calibrated using known hydraulic pressures in water columns.

Two needles were used in the experiment: one was for protecting the probe and the other was for generating a track in tissue. Since the probe is very fragile, it was inserted into the first needle (26 gauge, Bevel tip, Fisher Scientific, Springfield, NJ) with the probe tip advanced to the opening of the needle. Concerns were raised that the probe tip would be damaged during insertion into the tumor. Another identical needle was used before any IFP measurement to generate the same tissue track to allow easy insertion of the first needle with the IFP probe. After the track needle was withdrawn, the protection needle with the probe was inserted to the center of the tumor, and the measurement was recorded after local equilibrium. Then, the protection needle with the probe was withdrawn toward tumor periphery, and the IFP was measured at a tumor peripheral location half way between the center and the surface, similar to previous studies [14,15] where multiple IFP measurements were taken at different tumor depths. For each tumor, IFP was repeatedly recorded: baseline (before the heating), right after the 1-h heating, 2 h after the heating, and 24 h after the heating, as shown in Fig. 2, along the same needle track. All the

measurements were also performed on a tumor in the control group, side by side with the tumor in the experimental group to evaluate whether insertion of the pressure probe in tumors alters IFP reading.

2.3 MicroCT Scan and Analyses. Eight resected tumors ($n = 4$ in each group) were for microCT scan. They were scanned immediately after resection in a high-resolution microCT imaging system (Skyscan 1172, Micro Photonics, Allentown, PA). A tumor in the experimental group and a tumor in the control group were placed side by side in a low-density Styrofoam container to minimize photon absorption and prevent movement of tumors during scanning. A medium resolution scan was used with a pixel size of 17 μm (voxel size of 17 by 17 by 17 μm^3) and a power setting of 100 kV and 100 mA with no filter. Flat-field correction was used prior to each scan to minimize noise and artifacts. The scan time was approximately 90 min, and each scan resulted in over 1000 individual images.

The images obtained from the microCT imaging system were reconstructed using NRECON[®], a software package provided by micro photonics. The images were converted into a series of cross-sectional images (2000 pixels by 2000 pixels). Before reconstruction, parameters such as beam hardening, ring artifacts, and smoothing were adjusted to minimize artifacts. Throughout the study, constant reconstruction parameters were used. The resultant reconstructed images were GS images where the pixel intensities ranged from 0 being black to 255 being white.

The reconstructed images for either the control tumor or the experimental tumor were analyzed using in-house codes of MATLAB. Specifically, the nanoparticle distribution volume within a specific grayscale range from $GS = i * 10$ to $GS = (i + 1) * 10$, $i = 1, 2, \dots, 25$, which is calculated by counting all the voxels containing a grayscale number within that range, i.e., $N_{i*10, (i+1)*10}$, then multiplying it by the volume of the voxel. The nanoparticle distribution volumes over specific grayscale ranges were an indication of how uniform or nonuniform nanoparticles deposited in tumors. MATLAB codes were also used to visualize three-dimensional nanoparticle deposition regions in the tumors.

Our preliminary study has shown that the average grayscale number in a tumor without any nanoparticles was approximately 60. In this study, the grayscale value at a voxel (GS) exceeding this threshold grayscale value ($GS_{\text{threshold}}$) was considered as

proportional to the local nanoparticle concentration, assuming that the grayscale value has a linear relationship with the nanoparticle concentration [18]. The total amount of nanoparticles within a tumor is assumed proportional to the following mass index expression:

$$\text{Mass index} = \sum_{i=6}^K [(\overline{GS}_{i*10,(i+1)*10} - GS_{\text{threshold}}) * N_{i*10,(i+1)*10}] \quad (1)$$

where $\overline{GS}_{i*10,(i+1)*10}$ represents the average grayscale value within the grayscale range between $i*10$ and $(i+1)*10$ and K is the index of the last grayscale range with the highest particle concentration, and it depends on the scanned data of individual tumors.

2.4 Statistical Analyses. The results in individual groups are calculated and presented as mean \pm SD. Statistical evaluations between the control and heating groups were performed via the Student's t -test. Statistically significant difference between two individual groups was confirmed when the p -value was less than 0.05.

3 Results

The nanofluid was prepared by developing AuNPs functionalized with Fab fragments as active targeting moieties that specifically target the EphA2 receptor on PC3 cells (Fab fragment of the recombinant monoclonal antibody 1C1). Since high concentrations of AuNPs were needed for this study and to ensure stability of the AuNPs at such concentrations, dendronized AuNPs developed in Dr. M. Daniel's lab (AuNP-PPI-CO₂H) were used as starting AuNPs and then derivatized with Fab fragments designed for covalent attachment to AuNPs via click chemistry. Dendronized nanoparticles were functionalized with a linker displaying an azide termini needed for click chemistry with Fab-DBCO antibody fragments: this resulted in the formation of AuNP-PPI-linkerN₃ (see Fig. 1(a)). Finally, Fab-DBCO bearing the orthogonal alkyne functional group was attached to AuNPs through azide-alkyne click chemistry.

AuNP-Fab nanofluid was characterized using DLS and TEM. The hydrodynamic diameter (DLS size by number) of AuNP-PPI-CO₂H was 18 nm. After the addition of the linker, the overall nanoparticle size increased to 21 nm, and finally the size of AuNP-Fab reached 28 nm (see Fig. 1(b)): the 7 nm diameter increase closely matches the expected increase (7.4 nm) due to the Fab addition (3.7 nm on each side of the nanoparticle). Concerning the overall charge of the nanoparticles, AuNP-PPI-CO₂H displayed a zeta potential of around -40 mV, while AuNP-Fab's zeta potential was -31 mV in PBS. This evolution of zeta potential values again reflects the addition of Fab since zeta potential of Fab by itself is less negative (-13 mV). Moreover, in order to visualize the nanoparticles with their coating, we performed TEM with negative staining (see Fig. 1(c)): the thicker coating observed on AuNP-Fab compared to AuNP-PPI-CO₂H is another confirmation of the presence of Fab onto the nanoparticles surface.

The mice behaved normally in the heating chamber and tolerated the 1-h heating well with no observed adverse effects. Figure 4 shows the measured mouse body temperatures during the 1 h whole-body heating. It was found that the mouse body temperature increased quickly to 40 °C within the first 15 min and stabilized for the rest of the heating duration. Opening the door of the incubator briefly did not affect the mouse body temperature.

The tumor IFP before the heating is considered as the baseline pressure, and it varied from one tumor to another, with the average value and the standard deviation as 9.6 ± 8.5 mmHg ($n = 28$ including both center and periphery locations of 14 tumors). The baseline IFPs at the center (9.9 ± 7.7 mmHg, $n = 14$) were slightly bigger than that at the periphery (9.3 ± 8.1 mmHg, $n = 14$). Among the 14 IFPs measured at the baseline, the IFPs at the

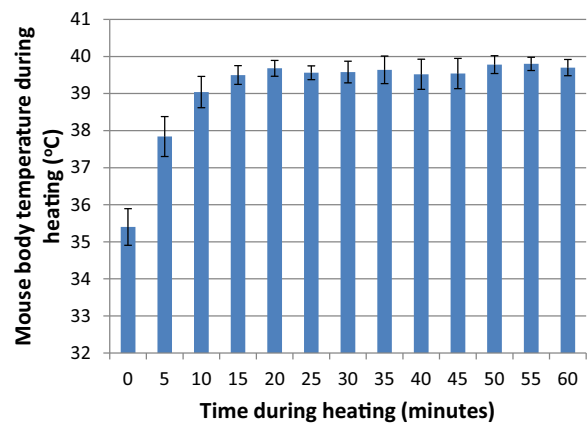


Fig. 4 Average values and standard deviations of the recorded mouse body temperatures during the 1 h whole-body heating

periphery location of ten tumors were lower than the IFPs at the center location.

Since the baseline IFPs in both tumor groups vary significantly, in this study, we normalized the IFPs from their baseline values as percentages of their baseline values. Figure 5 shows the IFPs at the center and periphery locations of the tumors in the control group without whole-body heating. Insertions and withdrawals of the needle and probe several times during the 25 h alone resulted in slight elevations of the IFP at the periphery and small decreases in the IFP at the center. The third column in each subgroup in Fig. 5 presents the average value of the IFPs at the two tumoral locations, and there is a minor change in the average IFP value in the control group from its baseline value.

On the contrary, in the experimental group with the 1-h whole-body heating, the IFP decreases approximately 45% from its baseline value immediately following the 1 h heating, as shown in Fig. 6. Two hours postheating, the IFP decreases 47% from the baseline, and the decrease is more evident at the tumor periphery. Twenty-four hours after the whole-body heating, the IFP rebounds slightly at the periphery location, while decreasing further at the center location. On average, the tumor interstitial pressure was 48% of its baseline value 24 h after the whole-body heating.

Statistical analyses were performed to evaluate whether the difference between the tumor groups with or without heating is statistically significant. Figure 7 shows the average pressure changes in the tumor groups with or without the 1-h whole-body heating. The normalized IFP from its baseline in the control group was always bigger in the tumors with the whole-body heating. Statistical significance indicated by the p -value less than 0.05 was confirmed

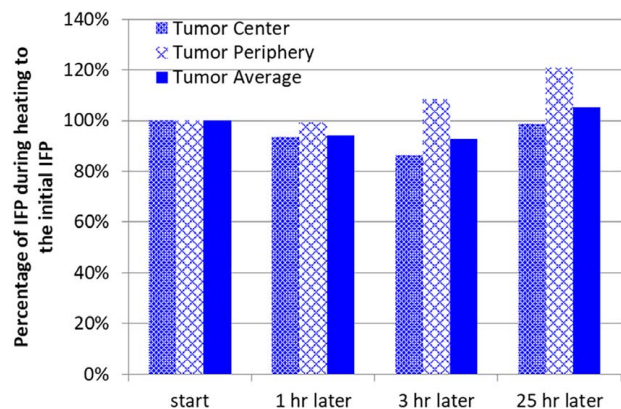


Fig. 5 Measured IFPs normalized by its initial pressure value in the tumors of the control group without the 1-h whole-body heating. IFPs at the center and periphery locations are averaged, represented by the third column.

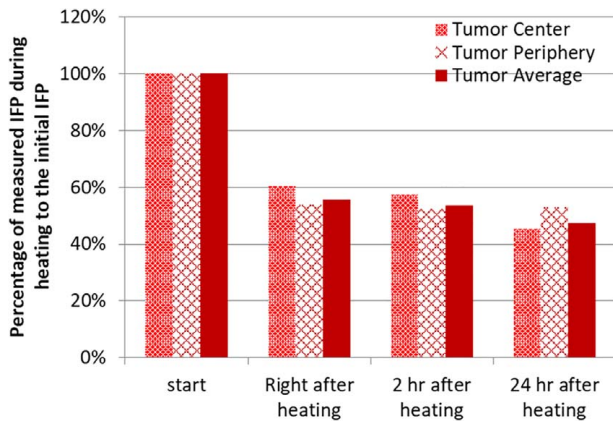


Fig. 6 Measured IFPs normalized by its initial value in the tumors of the experimental group with the 1 h whole-body heating. IFPs at the center and periphery locations are averaged, represented by the third column. IFP was measured four times: initial, right after the 1 h heating, 2 h after the heating, and 24 h after the heating.

right after the heating, 2 h, or 24 h after the whole-body heating between the normalized IFPs of the two groups.

The sizes of the tumors in both groups for the microCT scans were similar (experimental: $743 \pm 179 \text{ mm}^3$, $n=4$ versus control: $873 \pm 274 \text{ mm}^3$, $n=4$), calculated from the microCT scans via the total numbers of voxels and the known pixel size. Figure 8 shows slices of microCT scans of one tumor without nanofluid injection [24] and another tumor with nanofluid injection in the control group. Overall the gray scale values in the tumor with nanoparticles are much higher than that in the tumor without nanoparticles. Imaging analyses were performed to understand the total number of microCT voxels in individual grayscale ranges, i.e., 0–9, 10–19, 20–29 ... 250–255. As shown in Fig. 9, the maximal voxel number in all the grayscale ranges occurs at the grayscale range of 100–109, shifting from the average grayscale value of 60 in tumors without nanoparticle deposition. It is noted that there are more voxels in the ranges with higher grayscale values ($GS > 90$). If one considers that a high grayscale value is an indication of a high nanoparticle concentration, it is evident that there are more

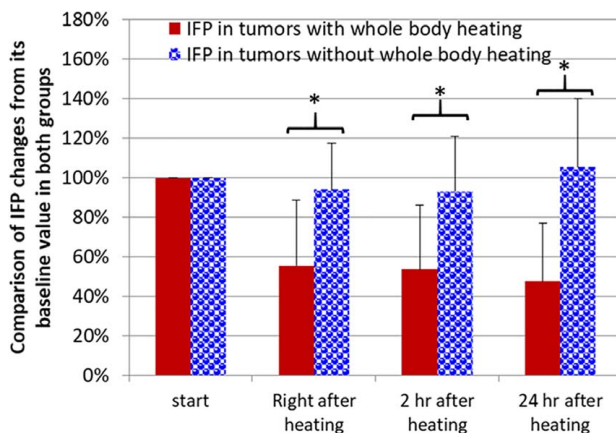


Fig. 7 Normalized IFPs from their baseline, based on the average IFP in each tumor. The solid columns represent IFPs in the control group, while the patterned columns represent IFPs in the experimental group with the whole-body heating. Error bars give the standard deviation of each group at different time instants. The symbol * denotes significant difference between the control and heating groups with a p -value less than 0.05.

nanoparticles delivered to the tumors after the 1-h whole-body heating than that in the tumors in the control group.

To understand where the nanoparticles were deposited in tumors, MATLAB codes were written to illustrate the 3D nanoparticle distribution regions. In Fig. 10, the black region represents tumor locations with nanoparticle deposition, where a higher grayscale value is considered as higher local nanoparticle concentration. As shown in Fig. 10, the top left 3D image shows a very small region at the tumor periphery containing nanoparticles at high concentrations, represented by a grayscale value larger or equal to 125, while there is no high concentration nanoparticle in the tumor center. At a lower cutoff grayscale value of 115, the occupied region of nanoparticles forms a partial spherical shell, again in the tumor periphery. Further lowering the cutoff grayscale value to 100, the occupied region forms a relatively complete spherical shell. However, nanoparticle penetration toward the tumor center cannot be seen when grayscale cutoff value is lower than 100, since the spherical shell blocks the visualization of nanoparticles inside.

The shell region with nanoparticle deposition at high concentrations can be better illustrated using only a central slice of the 3D visualization in Fig. 10. Figure 11 illustrates the gradual penetration of nanoparticles from the tumor periphery towards tumor center. Only nanoparticles at low concentrations (or low grayscale values in microCT images) are deposited in the tumor central region, and nanoparticles at high concentrations are mostly concentrated in the tumor periphery. If one compares the central slice of a tumor in the control group (left images in Fig. 11) to another tumor in the experimental group (right images in Fig. 11), it is evident that nanoparticles at higher concentrations occupy a bigger shell region with more penetration toward the tumor center than that in the control group.

The amount of the gold nanoparticle deposition was estimated based on the grayscale values in individual voxels. As shown Sec. 2, Eq. (1) was used to calculate the mass index, which is assumed proportional to the total amount of the gold nanoparticle deposition in tumors. Figure 12 presents the average and standard deviation of the mass index of all the tumors in both groups. The mass index of the tumors in the experimental group is 42% larger than that in the control group, implying that 42% more nanoparticles are delivered to the tumors due to the 1 h whole-body heating. The p value of 0.048 highlights the positive effect of 1-h whole-body hyperthermia on enhancing nanoparticle delivery to PC3 tumors.

4 Discussion

The current study was focused on evaluating whether a 1-h whole-body mild hyperthermia enhances targeted nanoparticle delivery to PC3 tumors. Here, microCT scans of tumors with nanoparticle distribution were used to quantify not only the total amount of nanoparticle deposition but also regional nanoparticle distribution in PC3 tumors. Unlike previous studies [14,15] where the IFP was measured only once at each tumor location, we measured IFP at each tumor location multiple times (before heating and several times after heating). Repeated measurements of IFP along the same path of the tumor before and after whole-body hyperthermia allowed us to minimize uncertainty of IFP recordings at random tumor locations. Recording IFPs in tumors in the control group without heating provides a sham control of incidental effect of inserting a pressure probe into tumors. However, potential measurement error of IFP may occur since the track needle might not be inserted into the same tissue track for each tumor. Nevertheless, similar to the previous studies using xenografted human head and neck tumors [15] and murine tumors [14], the current study has shown the effectiveness of the approach when applied to human PC3 tumors in mice. However, the results of the current study do not illustrate specific mechanisms of the decreases in IFP after whole-body hyperthermia. We speculate that the decrease in IFP

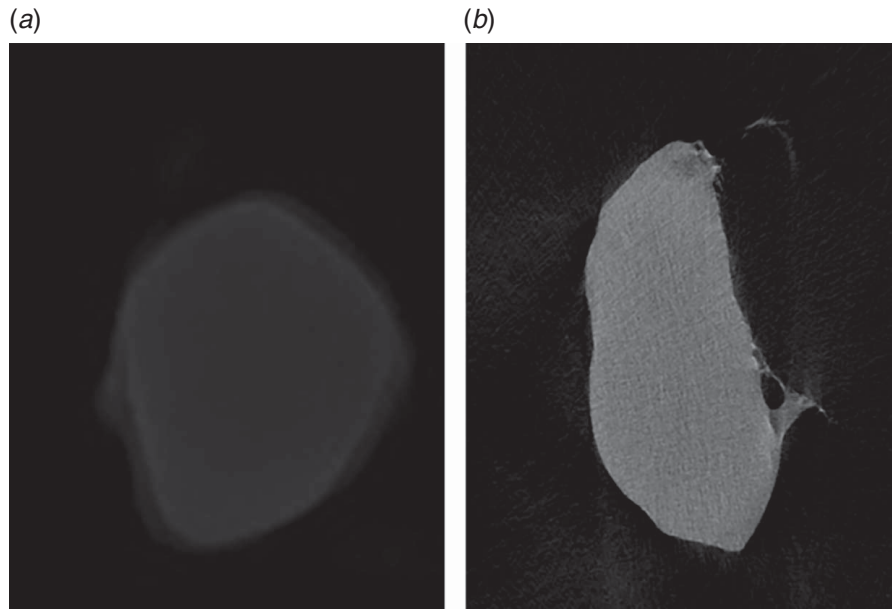


Fig. 8. (a) Grayscale microCT slices of a tumor without nanoparticles and (b) a tumor with nanoparticle deposition in the control group.

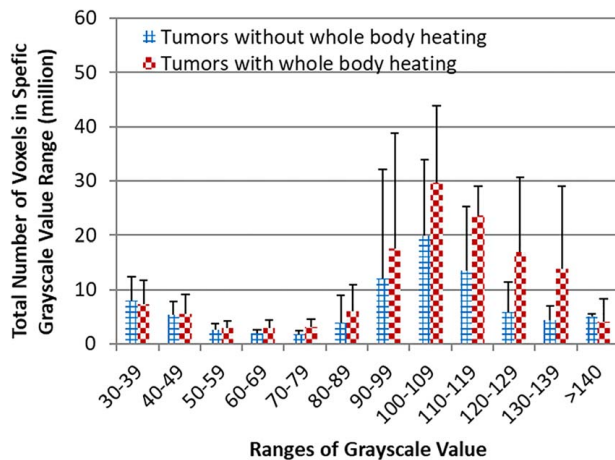


Fig. 9 The total number of voxels in a specific grayscale value range

may be due to improvement in lymphatic drainage. Lymphatic vessels contract when the temperature is reduced and dilate when the temperature is elevated. In physical therapy, taking a hot shower has been proposed to remove stagnant lymphatic fluid, thus, increase blood circulation [25]. However, this may be feasible only when tumors still have some partially functional intratumoral lymphatic vessels [26]. High solid stress in tumors has been observed in the previous study [27], and it is attributed to vessel compression and hypoperfusion in tumors. If whole-body hyperthermia modifies the solid stress, the originally collapsed intratumoral lymphatic vessels may be reopened to improve fluid drainage [28]. Other possible explanations of reduced IFP were suggested, including whole-body hyperthermia-induced thermoregulatory responses [15]. During whole-body thermal thermoregulation, systemically released neurovascular agents or signals may travel to the tumor to dilate various blood vessels, as an overall mechanism to dissipate heat to the surface of the body. Nevertheless, although more experiments are needed to illustrate the mechanisms, the correlation of reduced tumoral IFP to the increase in the total amount of nanoparticle deposition in tumors is evident from the current experiments.

Unlike local hyperthermia, whole-body hyperthermia is facile to implement and to control. Local hyperthermia to tumors, especially to deep-seated tumors, often leads to nonuniform heating. In traditional hyperthermia methods such as ultrasound, laser, microwave, etc., volumetric heat generation rate distribution induced by a heating device strongly depends on wave propagation and interaction between waves and tissue, and the distribution is often nonuniform with a larger volumetric heat generation rate at the superficial region. Hyperthermia treatment using injected magnetic nanoparticles subject to an alternating magnetic field is still affected by the nonuniform distribution of nanoparticle concentration in tumors [19]. On the contrary, whole-body hyperthermia elevates the temperature of the arterial blood circulating the entire body, and it typically results in a uniform temperature elevation in deep-seated tumors. The observed efficacy of enhanced nanoparticle delivery to PC3 tumors via the 1-h whole-body hyperthermia also provides a practical approach to implement in future clinical settings. The nontoxic 1 h whole-body hyperthermia would be more tolerated by patients/mice and would also lead to fewer systemic complications than that when 2–6 h of whole-body hyperthermia was implemented in previous studies.

MicroCT scan again demonstrates its feasibility of visualization and quantification of nanoparticle distribution in tumors. Nanoparticles, due to their higher density than tissue, have been shown in the past to appear as voxels in microCT images with much higher grayscale values. In our previous microCT studies on PC3 tumors injected with iron-based magnetic nanoparticles, the injection at the tumor center resulted in a white cloud in the image. Visual impression of the grayscale images in this study does not suggest a large chunk of density elevations in the tumors. This is very similar to one of our previous studies using gold nanorods in PC3 tumors in laser photothermal therapy [29]. It is possible that X-ray absorption by gold nanoparticles may be quite different from that by iron-based magnetic nanoparticles [19,29].

The current study is limited by the small sample size in each group. However, a tumor in the control group and a tumor in the experimental group were scanned together, minimizing fluctuation of microCT scan parameters. We believe that the observation of the larger regions of voxels containing higher nanoparticle concentration (i.e., larger grayscale value) in the tumor resected after whole-body hyperthermia than that in the tumor without heating affirms the credibility of the conclusion of this study. The overall elevation of microCT grayscale values in the tumors in the

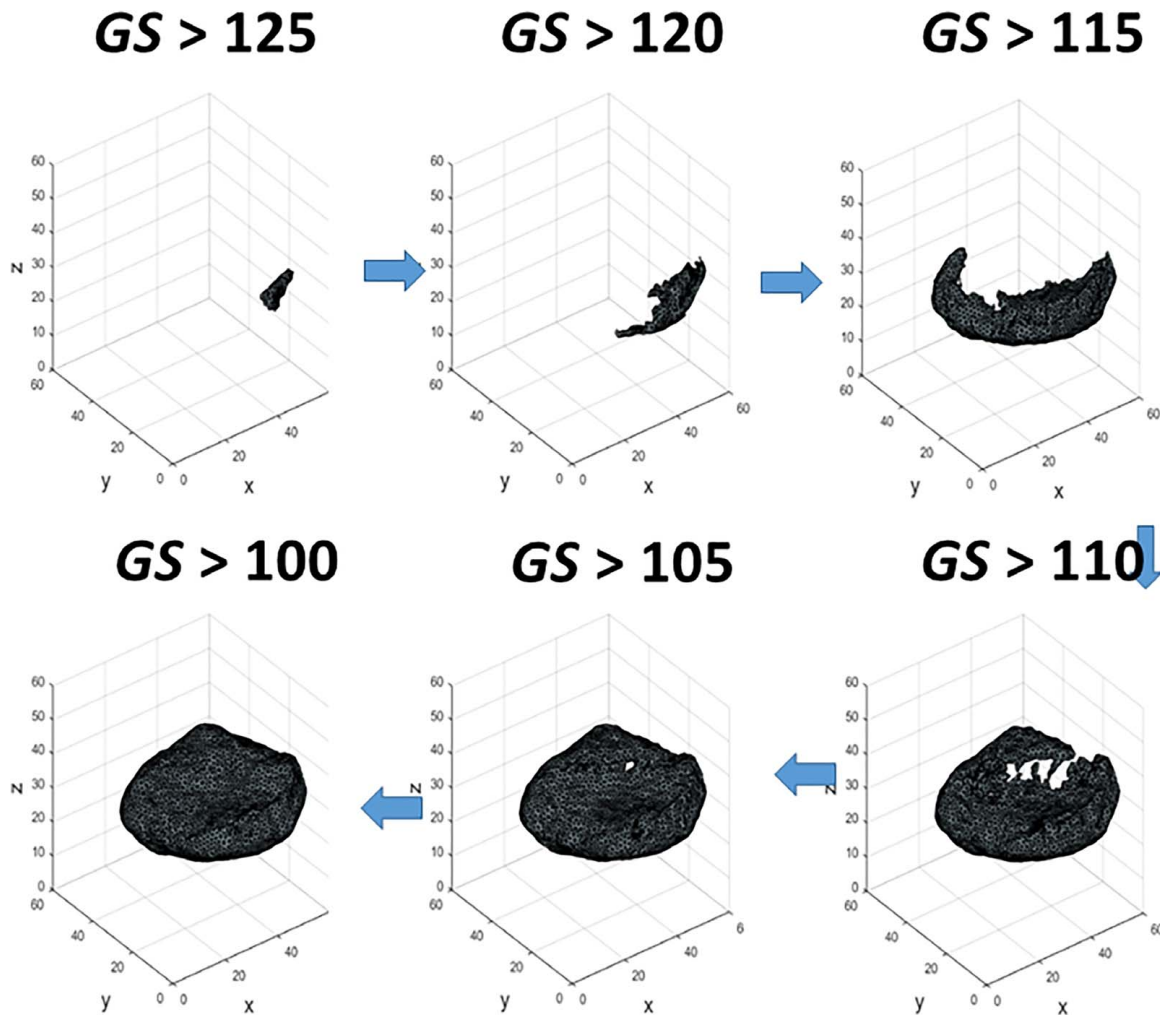


Fig. 10 3D nanoparticle deposition region using various cutoff grayscale values in a tumor

current study from that in tumors without nanoparticle deposition is a strong evidence of higher detectable absorption of X-ray by gold nanoparticles in tumors than the tumor tissue. Considering that nanoparticles have been used as drug carriers in medical research, one can take advantage of the X-ray absorption of nanoparticles to evaluate nanoparticle/drug distribution in tumors [1]. In the current study, the tumors were resected 24 h after the heating. Based on the information provided in a review article [30], the circulation half time of gold nanoparticles in BALB/c mice varies significantly from 6 h to 48 h, affected by the size of the nanoparticles. The circulation time of 24 h was selected to have the majority of the nanoparticle deposition in tumors before complete nanoparticle clearance in the blood stream. Future experiments could be performed to identify the optimal observation window to have the maximal nanoparticle deposition before nanoparticles are scavenged by the immune system of the body.

Results obtained from the microCT analyses of the resected PC3 tumors agree very well with previous studies. It is well known that IFPs in tumors are often elevated except at the tumor periphery. If the major driving force of the transvascular fluid/drug convection is the pressure difference between the pressure in the tumoral capillaries and the tumor interstitial space, more drug deposition should occur at the tumor periphery. Based on the microCT analyses, our experiments illustrate the same trend. Nanoparticles were deposited at higher concentrations in the tumor periphery than at the tumor center. This may be explained by the higher tumor IFP at the center than the IFP at the tumor periphery observed in most of tumors used in this study. Another possibility of increased

nanoparticle deposition at the tumor periphery is due to a larger number of tumor capillaries at tumor periphery. It is well documented that the tumor core region may be avascular or poorly perfused [31], which could lead to fewer nanoparticles delivered to the tumor central region. Unfortunately, the current study did not evaluate blood vessel distribution in tumors. Another factor that also may influence transvascular convection is the local blood perfusion rate. It was demonstrated in previous studies that whole-body hyperthermia increased openings of many capillaries in the tumor using fluorescence microscopy, implying an increase in local blood perfusion rate [15]. Tumoral blood perfusion rate on the tumor surface also resulted in significant increase using laser Doppler flowmetry [15]. It is the limitation of the current study that the local blood perfusion rate was not recorded.

In this current study, the microCT scan with a pixel size of $17 \mu\text{m}$ does not have the resolution higher than the size of a typical capillary in tumors; therefore, the scanned images cannot distinguish nanoparticles inside the circulation and nanoparticle extravasation in interstitial space. On the other hand, laser confocal fluorescence microscopy is an excellent imaging tool to focus on very small regions of vasculature in tumors, allowing visualization of capillaries and nanoparticles/drug extravasations from capillaries with a high submicron resolution [32]. Using fluorescence microscopy, a study by Li et al. demonstrated successful visualization of an endothelial lining gap (up to $10 \mu\text{m}$) induced by whole-body hyperthermia (41°C for 30 min) and enhancement in large-sized ($\sim 87 \text{nm}$ diameter) liposome extravasation and penetration into the interstitial space up to $27.5 \mu\text{m}$ from the vessel wall [11]. Winslow et al.

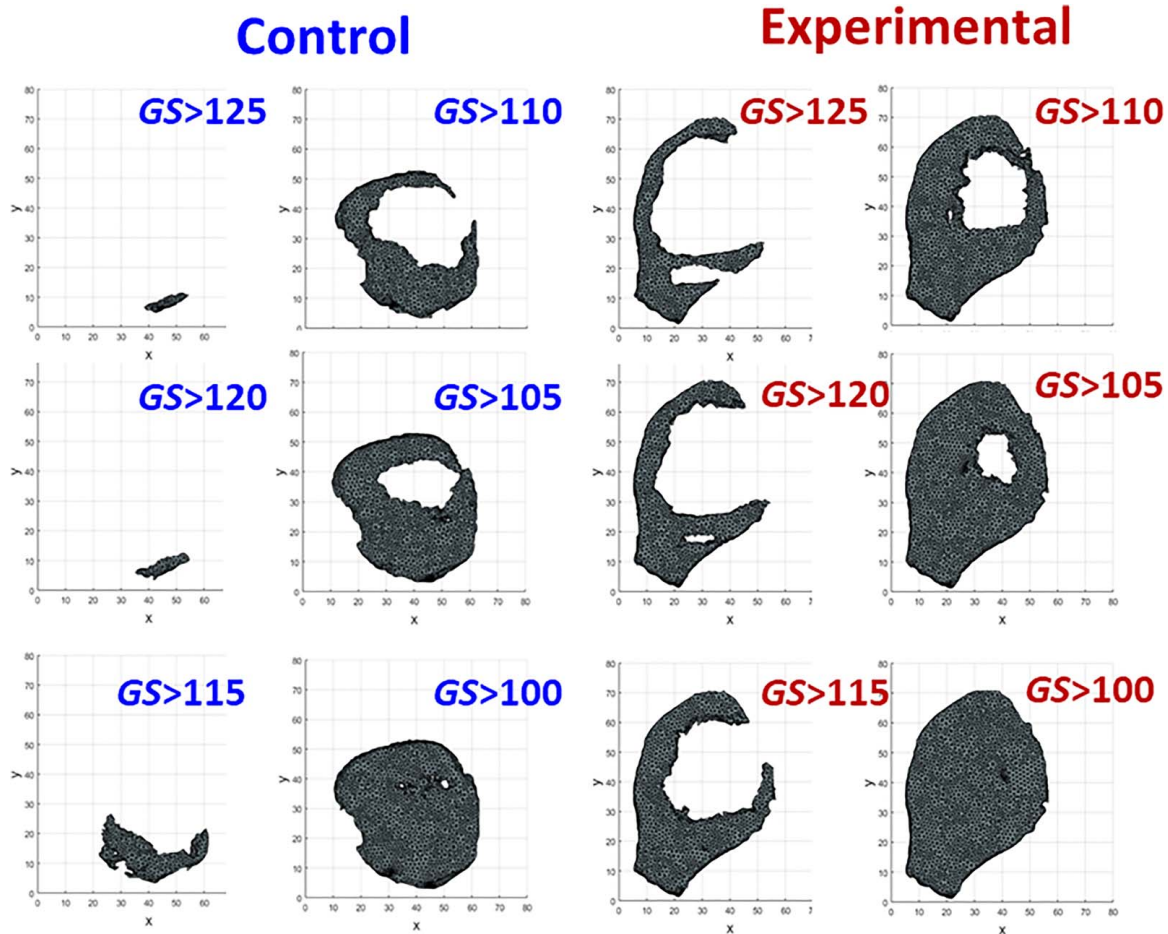


Fig. 11 Comparison of nanoparticle deposition penetration from tumor periphery to tumor center using a central slice of the 3D visualization of the tumors in the control group (top panels) and in the experimental group (bottom panels)

[15] enhanced liposome extravasation and opening of many blood vessels in the tumors after whole-body heating. However, penetration of confocal microscopy is limited to a tissue layer less than $200\ \mu\text{m}$ in thickness; thus, it cannot provide information of 3D vasculature and nanoparticle distribution in tumors. As shown in the current study, microCT scan is capable of quantifying the 3D grayscale value distribution. The grayscale value of a voxel location exceeding a threshold grayscale value may be considered

proportional to the local nanoparticle concentration, therefore, can be used to quantify both the local nanoparticle distribution and the total amount of nanoparticles deposited in tumors.

Another limitation of this study using microCT scan of tumors involved using 8-bit grayscale values ranging from 0 to 255. Any considerably larger local nanoparticle concentration would only register as the value of 255. The truncation underestimates the local nanoparticle concentration, and it may lead to a smaller value of the mass index than it actually is. In the future, 16-bit grayscale values would extend the scale range to 0–65,536; therefore, it is more accurate to quantify the nanoparticle concentration distribution in tumors.

In summary, in this study, we performed in vivo experiments on mice to evaluate whether whole-body hyperthermia enhances targeted nanoparticle delivery to PC3 tumors. The results show a decrease in the IFP of PC3 tumors after 1-h whole-body hyperthermia treatment, with an evident statistically significant reduction 2 h postheating and that was maintained for 24 h. Analyses of microCT scans of resected tumors show that nanoparticles at high concentrations are deposited mostly in the tumor periphery, while only nanoparticles at low concentrations are delivered to the tumor center. The 1-h whole-body hyperthermia leads to more presence of nanoparticle toward the tumor central region than that in the control group. The mass index calculated from microCT scan suggests overall 42% more nanoparticle delivery in the experimental group than that in the control group. The observed increase in targeted nanoparticle accumulation into tumors following mild hyperthermia treatment could be applied to improve current nanomedicines and nanobased tumor detection technologies.

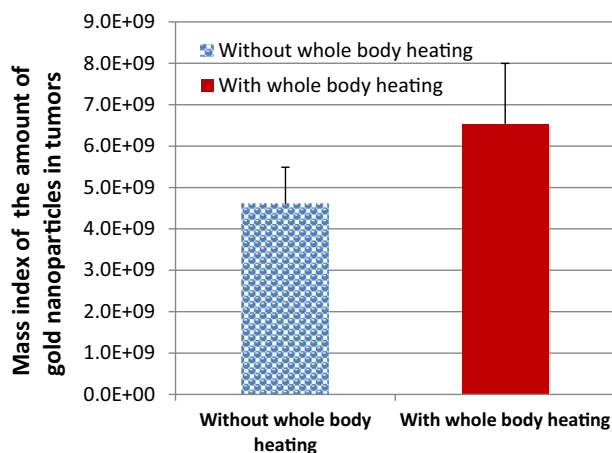


Fig. 12 Comparison of the calculated mass index between the control group without heating and the experimental group with 1 h whole-body heating

Acknowledgment

This research was supported by an NSF research grant (CBET-1705538). The research was performed in partial fulfillment of the requirements for the Ph.D. degree by Qimei Gu from the University of Maryland Baltimore County, Baltimore, MD. The authors are also thankful to Tagide deCarvalho for her assistance in sample preparation and acquisition of TEM images, and Ryan Fleming for expression and purification of the anti-EphA2 Fab protein.

References

- [1] Ghann, W. E., Aras, O., Fleiter, T., and Daniel, M.-C., 2012, "Syntheses and Characterization of Lisinopril-Coated Gold Nanoparticles as Highly Stable Targeted CT Contrast Agents in Cardiovascular Diseases," *Langmuir*, **28**(28), pp. 10398–10408.
- [2] Cheheltani, R., Ezzibdeh, R. M., Chhour, P., Pularparthi, K., Kim, J., Jurcova, M., Hsu, J. C., Blundell, C., Litt, H. I., Ferrari, V. A., Allcock, H. R., Sehgal, C. M., and Cormode, D. P., 2016, "Tunable, Biodegradable Gold Nanoparticles as Contrast Agents for Computed Tomography and Photoacoustic Imaging," *Biomaterials*, **102**, pp. 87–97.
- [3] Hirsch, L. R., Stafford, R. J., Bankson, J. A., Sershen, S. R., Rivera, B., Price, R. E., Hazle, J. D., Halas, N. J., and West, J. L., 2003, "Nanoshell-Mediated Near-Infrared Thermal Therapy of Tumors Under Magnetic Resonance Guidance," *Proc. Natl. Acad. Sci. USA*, **100**(23), pp. 13549–13554.
- [4] El-Sayed, I. H., Huang, X., and El-Sayed, M. A., 2006, "Selective Laser Photo-Thermal Therapy of Epithelial Carcinoma Using Anti-EGFR Antibody Conjugated Gold Nanoparticles," *Cancer Lett.*, **239**(1), pp. 129–135.
- [5] Cherukuri, P., Glazer, E. S., and Curley, S. A., 2010, "Targeted Hyperthermia Using Metal Nanoparticles," *Adv. Drug Delivery Rev.*, **62**(3), pp. 339–345.
- [6] Huang, X., Jiang, P., and Tanaka, T., 2011, "A Review of Dielectric Polymer Composites With High Thermal Conductivity," *IEEE Electr. Insul. Mag.*, **27**(4), pp. 8–16.
- [7] Eck, W., Craig, G., Sigdel, A., Ritter, G., Old, L. J., Tang, L., Brennan, M. F., Allen, P. J., and Mason, M. D., 2008, "PEGylated Gold Nanoparticles Conjugated to Monoclonal F19 Antibodies as Targeted Labeling Agents for Human Pancreatic Carcinoma Tissue," *ACS Nano*, **2**(11), pp. 2263–2272.
- [8] Stylianopoulos, T., Munn, L. L., and Jain, R. K., 2018, "Reengineering the Physical Microenvironment of Tumors to Improve Drug Delivery and Efficacy: From Mathematical Modeling to Bench to Bedside," *Trends Cancer*, **4**(4), pp. 292–319.
- [9] Baish, J. W., Netti, P. A., and Jain, R. K., 1997, "Transmural Coupling of Fluid Flow in Microcirculatory Network and Interstitium in Tumors," *Microvasc. Res.*, **53**(2), pp. 128–141.
- [10] Dreher, M. R., Liu, W., Michelich, C. R., Dewhirst, M. W., Yuan, F., and Chilkoti, A., 2006, "Tumor Vascular Permeability, Accumulation, and Penetration of Macromolecular Drug Carriers," *Int. J. Rad. Onc. Biol. Phys.*, **32**(5), pp. 1419–1423.
- [11] Li, L., ten Hagen, T. L. M., Bolkestein, M., Gasselhuber, A., Yatvin, J., van Rhooen, G. C., Eggermont, A. M., and Haemmerich, D., 2013, "Improved Intratumoral Nanoparticle Extravasation and Penetration by Mild Hyperthermia," *J. Controlled Release*, **167**(2), pp. 130–137.
- [12] Koning, G. A., Eggermont, A. M. M., Lindner, L. H., and ten Hagen, T. L. M., 2010, "Hyperthermia and Thermosensitive Liposomes for Improved Delivery of Chemotherapeutic Drugs to Solid Tumors," *Pharm. Res.*, **27**(8), pp. 1750–1754.
- [13] Chauhan, V. P., Stylianopoulos, T., Martin, J. D., Popovic, Z., Chen, O., Kamoun, W. S., Bawendi, M. G., Fukumura, D., and Jain, R. K., 2012, "Normalization of Tumour Blood Vessels Improves the Delivery of Nanomedicines in a Size-Dependent Manner," *Nat. Nanotechnol.*, **7**(6), pp. 383–388.
- [14] Sen, A., Capitano, M., Spornyak, J. A., Schueckler, J., Thomas, S., Singh, A., Evans, S. S., Hylander, B. L., and Repasky, E. A., 2011, "Mild Elevation of Body Temperature Reduces Tumor Interstitial Fluid Pressure and Hypoxia, and Enhances Efficacy of Radiotherapy in Murine Tumor Models," *Cancer Res.*, **71**(11), pp. 3872–3880.
- [15] Winslow, T. B., Eranki, A., Ullas, S., Singh, A. K., Repasky, E. A., and Sen, A., 2015, "A Pilot Study of the Effects of Mild Systemic Heating on Human Head and Neck Tumour Xenografts: Analysis of Tumour Perfusion, Interstitial Fluid Pressure, Hypoxia and Efficacy of Radiation Therapy," *Int. J. Hyperthermia*, **31**(6), pp. 693–701.
- [16] Pluen, A., Boucher, Y., Ramanujan, S., McKee, T. D., Gohongi, R., DiTomaso, E., Brown, E. B., Izumi, Y., Campbell, R. B., Berk, D. A., and Jain, R. K., 2001, "Role of Tumor-Host Interactions in Interstitial Diffusion of Macromolecules: Cranial vs. Subcutaneous Tumors," *Proc. Natl. Acad. Sci.*, **98**(8), pp. 4628–4633.
- [17] Monsky, W. L., Kruskal, J. B., Lukyanov, A. N., Girmun, G. D., Ahmed, M., Gazelle, G. S., Huertas, J. C., Stuart, K. E., Torchilin, V. P., and Goldberg, S. N., 2002, "Radio-Frequency Ablation Increases Intratumoral Liposomal Doxorubicin Accumulation in a Rat Breast Tumor Model," *Radiology*, **224**(3), pp. 823–829.
- [18] Attaluri, A., Ma, R., and Zhu, L., 2011, "Using MicroCT Imaging Technique to Quantify Heat Generation Distribution Induced by Magnetic Nanoparticles for Cancer Treatments," *ASME J. Heat Transfer*, **133**(1), p. 011003.
- [19] LeBrun, A., Joglekar, T., Bieberich, C., Ma, R., and Zhu, L., 2016, "Identification of Infusion Strategy for Achieving Repeatable Nanoparticle Distribution and Quantifiable Thermal Dosage in Magnetic Nanoparticle Hyperthermia," *Int. J. Hyperthermia*, **32**(2), pp. 132–143.
- [20] Gu, Q., Joglekar, T., Bieberich, C., Ma, R., and Zhu, L., 2019, "Nanoparticle Redistribution in PC3 Tumors Induced by Local Heating in Magnetic Nanoparticle Hyperthermia: In Vivo Experimental Study," *ASME J. Heat Transfer*, **141**(3), p. 032402.
- [21] Zabetakis, K., Ghann, W. E., Kumar, S., and Daniel, M.-C., 2012, "Effect of High Gold Salt Concentrations on the Size and Polydispersity of Gold Nanoparticles Prepared by an Extended Turkevich-Frens Method," *Gold Bull.*, **45**(4), pp. 203–211.
- [22] Saha Ray, A., Ghann, W. E., Tsoi, P., Szychowski, B., Dockery, L., Pak, Y., Li, W., Kane, M. A., Swaan, P. W., and Daniel, M.-C., 2019, "Set of Highly Stable Amine- and Carboxylate-Terminated Dendronized Au Nanoparticles With Dense Coating and Nontoxic Mixed-Dendronized Form," *Langmuir*, **35**(9), pp. 3391–3403.
- [23] Florinas, S., Liu, M., Fleming, R., Van Vlerken-Ysola, L., Ayriss, J., Gilbreth, R., Dimasi, N., Gao, C., Wu, H., Xu, Z. Q., Chen, S., Dirisala, A., Kataoka, K., Cabral, H., and Christie, R. J., 2016, "A Nanoparticle Platform to Evaluate Bioconjugation and Receptor-Mediated Cell Uptake Using Cross-Linked Polymer Complex Micelles Bearing Antibody Fragments," *Biomacromolecules*, **17**(5), pp. 1818–1833.
- [24] Gu, Q., Ray, A. S., Joglekar, T., Zaw, M., Daniel, M., Bieberich, C., Ma, R., and Zhu, L., 2018, "Feasibility of Visualization and Analyses of Deposition of Newly Developed Dendritic Ligand-Coated Gold Nanoparticles in PC3 Tumors Using MicroCT Scan," *ASME 2018 NanoEngineering for Medicine and Biology Conference*, Los Angeles, CA, Aug. 21–24, ASME Paper No. NEMB2018-6181.
- [25] Mariana, V. F., Maria de Fátima, G. G., and Maria, P., 2011, "The Effect of Mechanical Lymph Drainage Accompanied With Heat on Lymphedema," *J. Res. Med. Sci.*, **16**(11), pp. 1448–1451.
- [26] Leu, A. J., Berk, D. A., Lymboussaki, A., Alitalo, K., and Jain, R. K., 2000, "Absence of Functional Lymphatics Within a Murine Sarcoma: A Molecular and Functional Evaluation," *Cancer Res.*, **60**(16), pp. 4324–4327.
- [27] Stylianopoulos, T., Martin, J. D., Chauhan, V. P., Jain, S. R., Diop-Frimpong, B., Bardeesy, N., Smith, B. L., Ferrone, C. R., Hornicek, F. J., Boucher, Y., Munn, L. L., and Jain, R. K., 2012, "Causes, Consequences, and Remedies for Growth-Induced Solid Stress in Murine and Human Tumors," *Proc. Natl. Acad. Sci. USA*, **109**(38), pp. 4607–4612.
- [28] Baxter, L. T., and Jain, R. K., 1988, "Vascular Permeability and Interstitial Diffusion in Superfused Tissue: A Two-Dimensional Model," *Microvasc. Res.*, **36**(1), pp. 108–115.
- [29] Manuchehrabadi, N., Attaluri, A., Cai, H., Edziah, R., Lalanne, E., Bieberich, C., Ma, R., and Zhu, L., 2012, "MicroCT Imaging and In Vivo Temperature Elevations in Implanted Prostatic Tumors in Laser Photothermal Therapy Using Gold Nanorods," *ASME J. Nanotechnol. Eng. Med.*, **3**(2), p. 021003.
- [30] Nazanin Hoshyar, N., Gray, S., Han, H., and Bao, G., 2016, "The Effect of Nanoparticle Size on in Vivo Pharmacokinetics and Cellular Interaction," *Nanomedicine (Lond.)*, **11**(6), pp. 673–692.
- [31] Elming, P. B., Sorensen, B. S., Oei, A. L., Franken, N. A. P., Crezee, J., Overgaard, J., and Horsman, M. R., 2019, "Hyperthermia: The Optimal Treatment to Overcome Radiation Resistant Hypoxia," *Cancers*, **11**(1).
- [32] Popovic, Z., Liu, W., Chauhan, V. P., Lee, J., Wong, C., Greytak, A. B., Insin, N., Nocera, D. G., Fukumura, D., Jain, R. K., and Bawendiet, M. G., 2010, "A Nanoparticle Size Series for In Vivo Fluorescence Imaging," *Angew. Chem. Int. Ed. Engl.*, **49**(46), pp. 8649–8652.